Thermally activated helicity reversals of skyrmions

X. Z. Yu,[1,*] K. Shibata,[2] W. Koshibae,[1] Y. Tokunaga,[3] Y. Kaneko,[1] T. Nagai,[4] K. Kimoto,[4] Y. Taguchi,[1] N. Nagaosa,[1,2] and Y. Tokura[1,2]

[1]*RIKEN Center for Emergent Matter Science (CEMS), Wako 351-0198, Japan*

[2]*Department of Applied Physics and Quantum Phase Electronics Center (QPEC), University of Tokyo, Tokyo 113-8656, Japan*

[3]*Department of Advanced Materials Science, University of Tokyo, Kashiwa 277-8561, Japan*

[4]*Electron Microscopy Group and Transmission Electron Microscopy Station, National Institute for Materials Science, Tsukuba 305-0044, Japan*

(Received 2 December 2015; revised manuscript received 16 February 2016; published 14 April 2016)

Magnetic bubbles with winding number $S = 1$ are topologically equivalent to skyrmions. Here we report the discovery of helicity (in-plane magnetization-swirling direction) reversal of skyrmions, while keeping their hexagonal lattice form, at above room temperature in a thin hexaferrite magnet. We have observed that the frequency of helicity reversals dramatically increases with temperature in a thermally activated manner, revealing that the generation energy of a kink-soliton pair for switching helicity on a skyrmion rapidly decreases towards the magnetic transition temperature.

DOI: 10.1103/PhysRevB.93.134417

I. INTRODUCTION

Magnetic domain walls and bubbles have long been the subject of intensive studies, and have been applied to memory devices [1–4]. The focus in this work is the magnetic moment M^z parallel or antiparallel to the net ordered moments, which couples to the external magnetic field H^z and also conveys the information or signal. Hence the gradient of the magnetic field ∇H^z applies the forces and drives the domain walls or bubbles. On the other hand, recent advances in this subject are related to the transverse components M^x and M^y, which bring about the topological nature of the magnetic bubbles and the magnetization textures in general. A magnetic bubble is regarded as a closed loop of the domain wall, which separates the regions $M^z < 0$ inside and $M^z > 0$ outside. The transverse components M^x and M^y appear in the domain wall region, and its behavior defines the two degrees of freedom, i.e., helicity and vorticity [5].

Let ϕ be the polar angle measured from the center of a bubble, and define $\psi(\phi)$ as the magnetization in the plane of (M^x, M^y), i.e., $M^x = M\cos\psi(\phi)$, $M^y = M\sin\psi(\phi)$ along the domain wall (Fig. 1). The vorticity is defined as the direction of the rotation of the transverse magnetic moments and is represented by the winding number $S = \frac{1}{2\pi}\int_{\phi=0}^{2\pi} d\psi(\phi)$. This winding number is directly related to the skyrmion number $N_{\rm Sk} = \iint \frac{dxdy}{4\pi}\vec{n}\cdot(\frac{\partial\vec{n}}{\partial x}\times\frac{\partial\vec{n}}{\partial y})$ defined as the wrapping number of a unit sphere for the mapping from the two-dimensional real space to the unit sphere of the magnetization direction $\vec{n} = \vec{M}/|\vec{M}|$. One can easily see that $N_{\rm Sk} = -S$ when $M^z < 0$ in the core and $M^z > 0$ in the periphery of the skyrmion and the bubble. This defines the topology of the bubble, and we call the bubbles with finite $N_{\rm Sk}$ skyrmions. Therefore some of the bubbles are skyrmions, while the others are trivial ones. Hard bubbles with $S \gg 1$ are necessarily skyrmions in our definition. In particular, the magnetic skyrmion as recently realized in chiral-lattice magnets [6–8] holds promise in the development of spintronics [9,10] because of its topological stability and function as the nanometric magnetic particle characterized by $N_{\rm Sk}$ [5]. The skyrmionic topological magnetization textures can be found not only in chiral-lattice magnets exhibiting a Dzyalloshinskii-Moriya interaction (DMI), but in thin plates of ferromagnets with uniaxial magnetic anisotropy as well [11,12]; in the latter, the hexagonal lattice form of magnetic bubbles as well as the linear domain-wall stripe is stabilized via the magnetic dipolar interaction [5,11–13].

On the other hand, the helicity is defined as the absolute value of φ (see the definition of φ in Fig. 1) and we are not concerned with the direction of its change. For example, any constant value of φ gives $N_{\rm Sk} = -S = -1$. $\varphi = \pm\pi/2$ corresponds to the skyrmion with a Bloch wall, while $\varphi = 0$ or π corresponds to that with a Néel wall, which is energetically unfavorable. Hereafter, the sign $\pm$ for the magnetic helicity is used to represent the in-plane magnetization-swirling direction on the Bloch domain wall. The skyrmions ($S = 1$ bubbles) with $\pm$ helicities produced by dipolar interaction are degenerate in energy for centrosymmetric (achiral) magnets, whereas the skyrmion helicity in the chiral-lattice magnet is uniquely determined by the sign of the DMI. Thus the helicity in the $S = 1$ bubble of a centrosymmetric magnet is viewed as an additional degree of freedom of the skyrmion [5,14].

Since the $S = 1$ bubble is identified as the skyrmion [5,11], the thermal stability or fluctuation of the topological property is an important issue to be investigated. Analogous to the chemical reaction accelerated at higher temperatures [15], the thermally activated magnetization reversal has been theoretically anticipated in nanomagnetic particles [16,17], and has also been experimentally confirmed for an isolated skyrmion realized in a superparamagnet [18]. However, the helicity dynamics in the magnetic bubbles or skyrmions remains elusive, particularly in the case of their lattice form. In this study, combining the quantitative analyses of spatially and temporally resolved data of Lorentz transmission electron microcopy (LTEM) with numerical simulation, we have found the thermally activated helicity reversals for the spontaneous bubble lattice [zero-field bubble lattice (SkL) phase] in the (001) thin plate of a hexaferrite crystal, $BaFe_{12-x-0.05}Sc_xMg_{0.05}O_{19}$

*To whom correspondence should be addressed: yu_x@riken.jp

 ©2016 American Physical Society

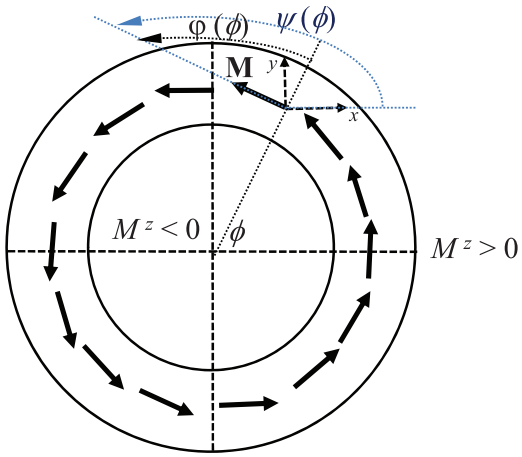

FIG. 1. Schematic of a bubble with winding number 1. Arrows show that the magnetic moments and concentric rings are a bubble domain wall. ϕ, φ, and ψ denote the polar angle, azimuthal angle, and the angle between the magnetic moment and the x direction, respectively.

($x = 1.8$) (BFSMO). It is observed that the helicity reversals for an individual skyrmion occur in a thermally activated manner approaching the Curie temperature ($T_C \sim 450$ K), while keeping the SkL intact.

II. EXPERIMENT

A BFSMO single crystal was grown by the floating zone technique. The phase purity and magnetic properties of the bulk sample were confirmed to be identical with those reported in the literature [19]. A (001) thin plate was cut from a bulk sample, the orientation of which was determined by means of Laue diffraction. For the LTEM sample, we thinned the (001) plate to a thin film form with a thickness below 100 nm by mechanical polishing and ion-beam milling using a Gatan precision ion polishing system (PIPS) operated with an acceleration voltage of 4 kV at room temperature (RT). The crystalline orientation of the thin film was also checked by the selected-area electron diffraction technique. The thickness of the observed film was measured by electron energy-loss spectroscopy [20].

To observe an $S = 1$ bubble lattice we utilized real-space observation by LTEM. LTEM allowed the in-plane magnetization to be imaged as convergence (bright contrast) or divergence (dark contrast) of the electron beam on the defocused image planes [20]. The inversion of magnetic contrasts can be discerned between the over- and underfocus images. However, the out-of-plane magnetizations parallel to the incident electron beam cannot be measured using LTEM. The zero-field-bias magnetic configurations can be explored by turning off the magnetic-objective lens current of a standard transmission electron microscope (JEOL, JEM-2800). The smallest remnant magnetic field is below 10 Oe after performing a degaussing operation for the microscope [21].

III. RESULTS AND DISCUSSION

First, we discuss the zero-field SkL at RT, coexistent with the stripe domains in a (001) BFSMO thin plate with a thickness of <100 nm. Figure 2(a) represents defocused LTEM images observed at RT and zero magnetic field. By analyzing the two defocused LTEM images with the transport-of-intensity equation (details are given in Appendix A) [22], we obtained the magnetization textures for the SkL as well as the stripe domains as shown in Fig. 2(b). The magnified textures shown in Figs. 2(c) and 2(d) for the bubbles surrounded by dotted squares in Figs. 2(a) and 2(b) clearly indicate two hexagonally shaped bubbles with the topological number $S = 1$, while they show opposite helicities. Accordingly, the dark/white hexagonally shaped bubble shown in Fig. 2(a) can be viewed as the skyrmions with + and − helicities, respectively. We have also performed the LTEM observations under external magnetic fields applied perpendicularly to the plate plane. It is observed that the field transforms the hexagonally-shaped bubbles into the curved stripe domains and then to the bubbles with the usual circular shape [see Figs. 6(b)–6(d) in Appendix B]. Upon further increasing the magnitude of field, the whole area is observed to be simply magnetized along the field direction [Fig. 6(e) in Appendix B]. When the field direction is reversed, interestingly the same bubble-stripe-bubble transformation occurs while accompanying random helicity reversals of bubbles [Figs. 6(f)–6(h) in Appendix B]. Systematic LTEM observations with variations of the sign and magnitude of the normal magnetic field have confirmed the formation of the zero-bias-field SkL at RT in the (001) BFSMO thin plate. Hereafter, we focus on the dynamics of the skyrmionic bubbles only under zero magnetic field.

The thermally activated excitation of bubble helicity reversals has been observed with the increase of temperature from RT up to near T_C [see Movie S1 in the Supplemental Material (SM) [23]]. Figures 2(e)–2(h) and 2(i)–2(l) are snapshots of raw LTEM data (Movie S2) for several time points at 433 K and the same data with markers denoting the +/− helicity, respectively. The bubble with +/− helicity shows up as dark/white rings in the LTEM contrast images shown in Figs. 2(e)–2(h). The helicity of one bubble [marked by yellow arrows in Figs. 2(f)–2(h)] was observed to sequentially reverse from plus to minus and then to plus during 1 s at 433 K. As we increase the temperature up to 437 K, most of the bubbles dynamically and randomly reverse their helicities [see Figs. 2(m)–2(t) and Movie S3], while maintaining the hexagonal SkL. The helicities for some bubbles or their LTEM contrast images become barely distinguishable [see the bubbles marked by violet balls in Figs. 2(q)–2(t)], suggesting that the frame rate of the LTEM movie (30 fps) is much lower than the helicity-reversal frequency.

Each frame in the above-mentioned movies contains physical information averaged over the exposure time (33 ms). To investigate the temperature-dependent dynamics of helicity reversal, we apply principal component analysis (PCA) [24] to the LTEM movies including 66 bubbles as indexed in Fig. 3(a). The detailed procedure for, and explanation of, the PCA are described in Appendix C. For each bubble, we calculate the first principal component, which is expected to represent the intensity distribution of a magnetic bubble and, hence, to be related to the bubble helicity because helicity reversal is supposed to be the largest intensity change in the movies. Figures 3(b) and 3(c) show the principal component

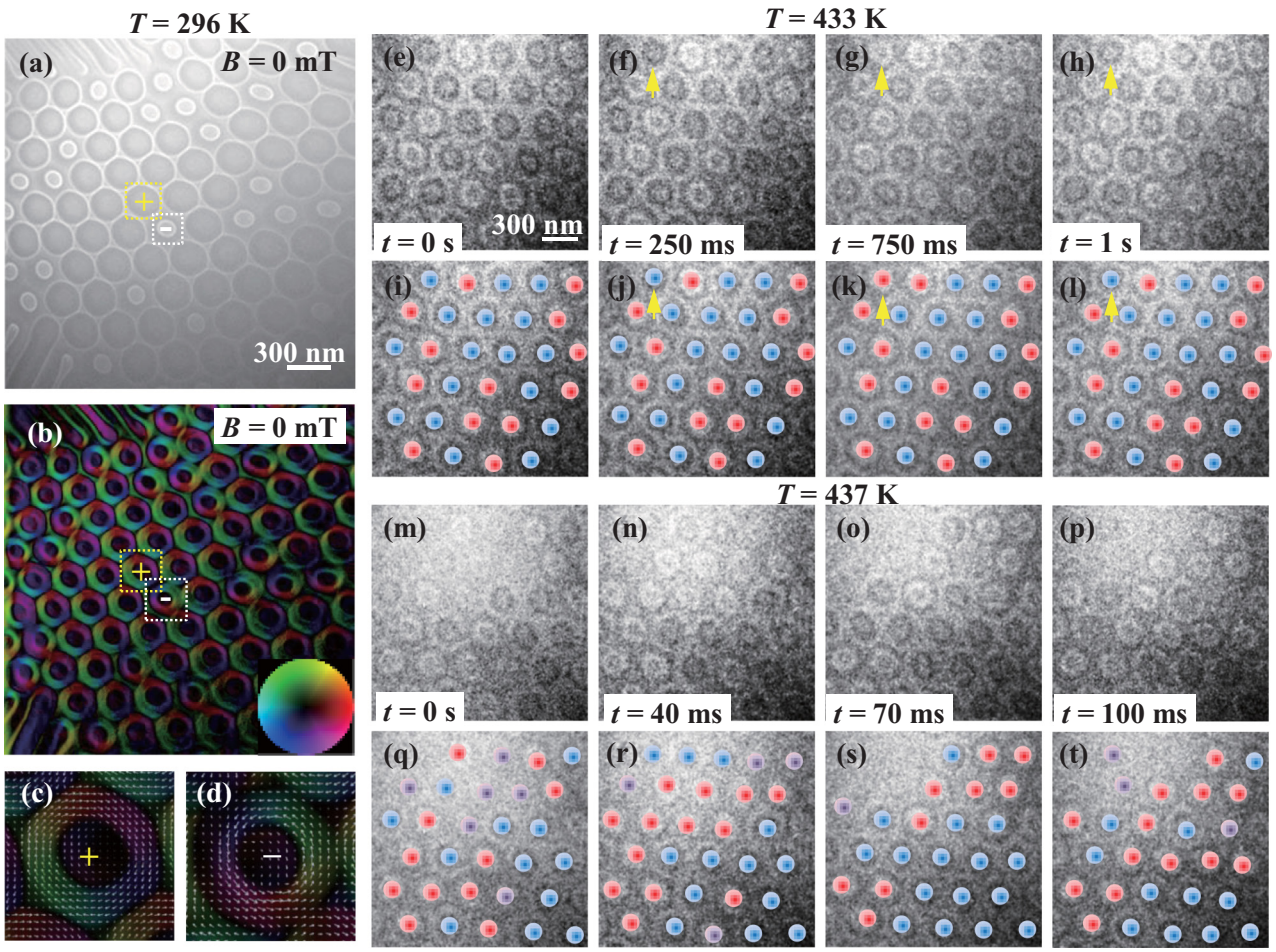

FIG. 2. Real-space observations of zero-field room-temperature skyrmions ($S = 1$ magnetic bubbles) and their dynamical helicity reversals in a (001) $BaFe_{12-x-0.05}Sc_xMg_{0.05}O_{19}$($x = 1.8$) thin plate (sample thickness is below 100 nm). (a), (b) Underfocused LTEM image and the corresponding in-plane magnetization texture obtained under zero-field bias at room temperature (296 K). (c), (d) Magnified images of two bubbles indicated with dotted squares in (b). Color wheel and arrows indicate the magnitude and direction of the in-plane magnetizations, while the dark color in (b)–(d) shows the out-of-plane magnetizations. "+" and "−" denote clockwise and counterclockwise helicities of the bubbles, respectively. (e)–(t) Snapshots of *in situ* LTEM movies observed at (e)–(l) 433 K and (m)–(t) 437 K. The lower panels [(i)–(l) and (q)–(t)] with markers are the same as the upper panels [(e)–(h) and (m)–(p)]. The yellow arrow indicates the bubble whose helicity changes in every frame. The light blue and red balls indicate bubbles with + and − helicities, respectively, while the violet balls indicate the traces of bubbles whose helicities are hardly observable due to the rapid helicity reversal events.

images related to a typical principal eigenvector and its inverse vector (see Appendix C for details), respectively. Two clear concentric rings with bright and dark intensity indicate that the statistical analyses filtered out background noise in the LTEM movies and that the helicity reversal causes a linear intensity change. Although the sign of the eigenvectors can be taken as arbitrary, the sign corresponds to the physical information, i.e., the bubble helicity in this case. To evaluate the helicity, here we choose the sign of each eigenvector so that it presents the intensity distribution of the + helicity, while its inverse corresponds to the − helicity. For some bubbles in the LTEM movies, however, the image corresponding to the principal eigenvector does not show the intensity distribution of a bubble as exemplified in Fig. 3(d). Such bubbles are excluded from the following analyses since we cannot extract any information on bubble helicity.

Figure 3(e) shows the analyzed time dependence of the score (h) (see the description in Appendix C) representing the frame-averaged helicity for the 66 indexed bubbles shown in Fig. 3(a) at several temperatures. We plot the value of h in a blue-white-red gradation. Since we take the sign of the first principal eigenvectors so that it corresponds to the + configurations, positive and negative values of h correspond to the + and − bubble helicities, respectively. Gray denotes the unanalyzed cases due to the inappropriate eigenvectors, such as that corresponding to the image shown in Fig. 3(d). These analyses qualitatively demonstrate that the frequency of helicity reversal and the population of the bubbles accompanying helicity reversal increase with temperature. At a temperature of 433 K, the helicity reversals are discerned only for a few bubbles; Upon increasing the temperature to 435 K, the helicities for approximately one-third of the bubbles change within 6.7 s; The frequency and the number of bubbles accompanying the helicity reversal increase with a further increase of temperature to 437 K; at a higher temperature of 439 K near $T_C \sim 450$ K, almost all of the analyzed bubbles reverse their helicities rapidly, and the helicities for some

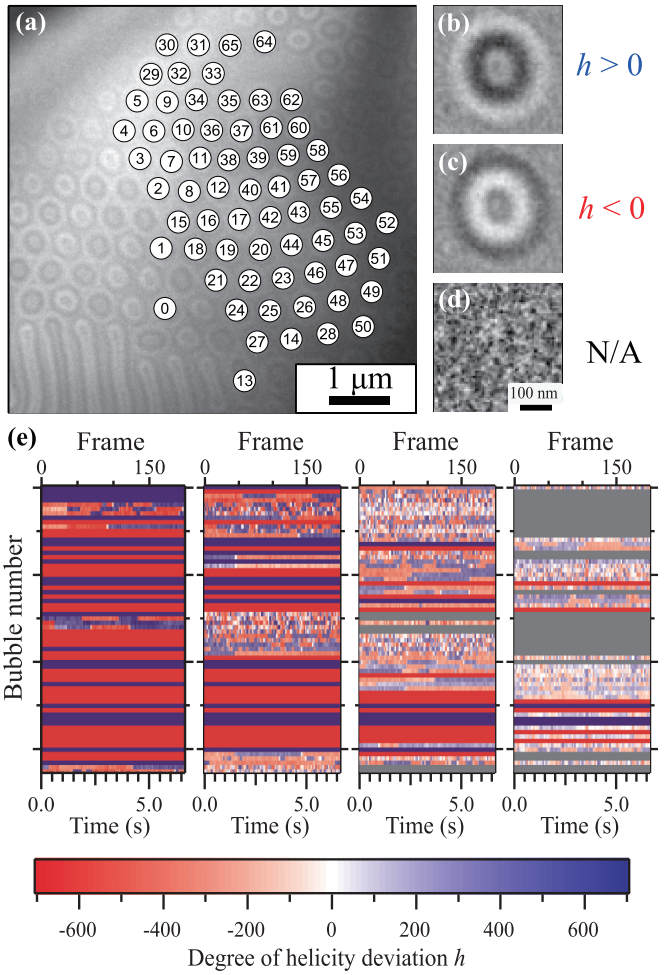

FIG. 3. Principal component analysis (PCA) of intensities of bubbles in LTEM movies. (a) Time-averaged image of a LTEM movie of duration 6.7 s observed at 433 K and 0 T. The numbered bubbles were selected for the PCA analyses. Images corresponding to the first principal eigenvectors obtained by the PCA on a typical bubble (No. 3) at (b) 435 K and (d) 439 K. (c) Image corresponding to the inverse vector of (b). The intensity distributions of (b) and (c) correspond to + and − helicity bubbles, respectively. The noisy intensity distribution of (d) is ascribed to the apparent average of intensity of a bubble with rapid helicity reversals within the exposure time. (e) Time dependence of the analyzed score h, which corresponds to the apparent average of helicity deviation, for 66 bubbles at various temperatures. The score h is plotted in a red-white-blue gradation. Blue and red correspond to the positive and negative values of h, which means that the helicity assumes + and − configurations, respectively. White indicates the middle value $h = 0$, which corresponds to the middle value between + and − configurations, with no deviation in the apparent average of helicity. For the bubbles which show no helicity reversal over the duration of the movies, their helicities are checked by intensity distribution in LTEM movies and the corresponding colors are allotted. Gray represents undeterminable helicity due to inappropriate eigenvectors, such as drifting or deformation of a bubble.

bubbles become undeterminable with inappropriate eigenvectors, suggesting that the helicity-reversal speed exceeds the frame rate (30 fps) of the LTEM movie.

To discuss the thermal activation energy of the helicity reversal, we focus on one representative bubble (No. 3).

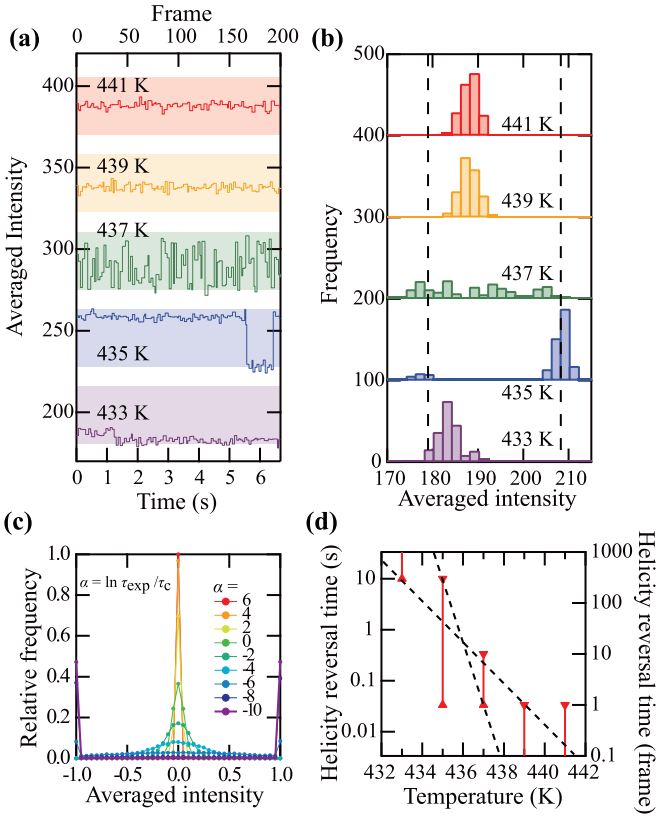

FIG. 4. Analyses of helicity reversal time with increase of temperature. (a) Averaged intensity of the LTEM inner circle image of bubble No. 3 [see Fig. 2(a)] as a function of time. The lower and upper edges of the colored band at each temperature denote the expected intensity for the + and − helicity bubbles in the static limit, respectively. (b) Histogram of the averaged intensity for bubble No. 3 at various temperatures. The left- and right-hand vertical dashed lines represent the intensities corresponding to the + and − helicity bubbles in the static limit. Data obtained at different temperatures in (a) and (b) are shifted vertically by 50 and 100, respectively, for visibility. (c) Simulated histogram of frame-averaged intensity for various ratios of the exposure time (τ_{exp}) to the helicity reversal time (τ_c). (d) Temperature dependence of typical helicity reversal time for the bubble (No. 3). The two dashed lines represent the fits to the thermal activation formula $\tau(T) \propto \exp\{\frac{E_{act}(T)}{k_B T}\}$, with the largest and the smallest inclination within the error range (see the main text).

Figure 4(a) shows the time and temperature dependences of the averaged intensity for the inner ring of the bubble (bubble domain wall) shown in Fig. 3(a): The period of helicity reversals becomes shorter with increasing temperature, and the averaged intensity becomes almost constant at $T \geqslant 439$ K. Figure 4(b) shows the histograms of the averaged intensity of the bubble during a period of 6.7 s at various temperatures. The changes of the histograms with temperature are as follows: One peak corresponding to a fixed helicity is observed at 433 K; two peaks corresponding to + and − helicities appear with increasing temperature to 435 K; and the histogram becomes flat and no significant peak is observed at 437 K, indicating that the helicity reverses frequently. This can be interpreted in terms of the concept of motional narrowing. The simulated frame-averaged intensity histograms for the various ratios between the helicity-reversal time (τ_c) and the exposure (observation)

time ($\tau_{\rm exp}$) are shown in Fig. 4(c). When $t_c \gg t_{\rm exp}$, the intensity corresponding to +/− helicity can be identified by the two peaks at ±1. Meanwhile, when $t_c \ll t_{\rm exp}$, the rapid intensity change between + and − helicities averages out the intensity in each frame, yielding the single peak at 0. This feature is in accord with the observed change in the histograms shown in Fig. 4(b) with increasing temperature. Figure 4(d) plots the temperature dependence of the typical time for helicity reversal (τ) estimated by combining the experimental results shown in Fig. 4(a) with the comparison of histograms of frame-averaged intensity obtained by *in situ* LTEM observations shown in Fig. 4(b) and Monte Carlo simulations shown in Fig. 4(c) (see Appendix D for details). Based on the common Arrhenius law, $\tau(T) \propto \exp\{\frac{E_{\rm act}(T)}{k_B T}\}$ (where k_B is Boltzmann's constant), we can estimate the thermal activation energy $E_{\rm act}$ as

$$430 \times k_B|T_C - T| < E_{\rm act}(T) < 1300 \times k_B|T_C - T|. \quad (1)$$

$E_{\rm act}$ is on the order of 1 eV at $T = 435$ K and decreases with increasing temperature toward $T_C \sim 450$ K.

Here we discuss the modeling and simulation for the microscopic process of the thermally activated helicity reversal in the bubble with topological number −1. The original model [12] includes three energy scales, i.e., the exchange energy A, the dipolar coupling $2\pi M^2$, and the anisotropy energy K. The ratios of these energy scales determine the two length scales, i.e., the width (ξ) of the domain wall $\xi = \sqrt{A/K}$ and that (λ) of the Bloch line (BL) along the domain wall $\lambda = \sqrt{A/(2\pi M^2)}$ in a unit of the lattice constant $a = 1$. The quality factor Q is defined as the ratio of the anisotropy energy and the dipolar coupling as $Q = K/(2\pi M^2)$, and the bubble formation is possible only when $Q > 1$. In the high-Q limit, the effective Hamiltonian of the magnetic moments along the domain wall is expressed by

$$H = 2\xi d_c \oint d\phi \left\{ \frac{1}{R} A[\partial_\phi \varphi(\phi)]^2 - 2\pi M^2 R \sin^2\varphi(\phi) \right\}, \quad (2)$$

where d_c is the number of magnetic layers, R is the bubble radius, and $\varphi(\phi)$ represents the in-plane direction of the magnetic moment at the angle ϕ as mentioned above (also see Fig. 5 and Appendix E). The dipolar energy prefers the Bloch wall, i.e., $\varphi = \pm\pi/2$, and the BL along the vertical direction corresponds to the kink connecting the two regions $\varphi = \pi/2$ and $\varphi = -\pi/2$. The energy of a BL ($E_{\rm BL}$) per magnetic layer is estimated as $E_{\rm BL} = 8AQ^{-1/2}$ [12]. We estimate the activation energy $d_c E_{\rm BL} \approx 1.8$ eV by extrapolating the formula for $Q \gg 1$ to $Q \sim 1$, assuming the values of $T_C - T = 15$ K and $d_c = 170$ (for sample thickness 50 nm, c-axis lattice constant 2.36 nm, and eight magnetic layers in a unit cell). (See Appendix E for details of the calculation.) This compares well to the observed value. On the other hand, in order to introduce the change in the winding number S or skyrmion number, one must introduce the singularity of the magnetization configuration. More explicitly, the width of the domain wall should be reduced to an atomic scale at some points, whose energy cost is of the order of A and larger than that of the BL. Therefore, this process is negligible compared with those without changing S. In the following, we show that the pair creation and annihilation of

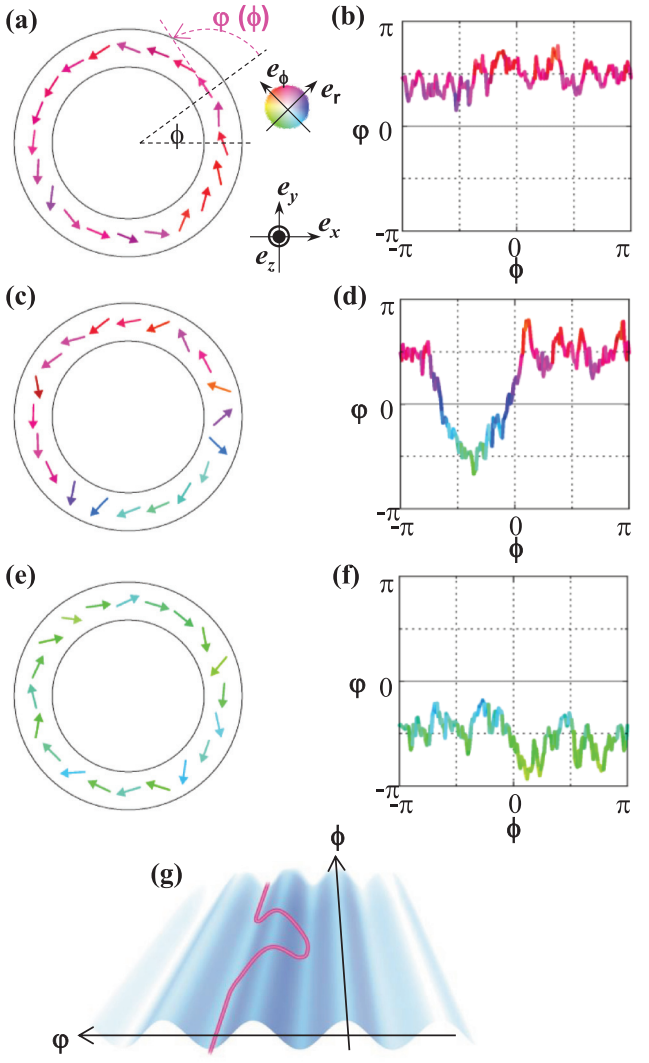

FIG. 5. Numerical simulation demonstrating the helicity reversal by thermal agitation. The simulation is based on the stochastic Landau-Lifshitz-Gilbert equation for the discretized model of N-magnetic moments on the one-dimensional ring (see Appendix E for detail). (a), (c), and (e) Magnetization textures during the helicity reversal. The color coding is defined by the basis vectors $\boldsymbol{e}_r$ in the radial direction and $\boldsymbol{e}_\phi$ in the circumferential direction. The arrows indicate the magnetic moments at the 20 sites out of $N = 200$. (b), (d), and (f) Corresponding profiles of the angle $\varphi(\phi)$ of (a), (c), and (e). The angle $\varphi(\phi) = \pi/2\,(-\pi/2)$ corresponds to the − (+) helicity. (g) Schematic of the helicity reversal by the creation and annihilation of kink-antikink pairs of the phase angle $\varphi(\phi)$.

BLs cause the helicity reversal without changing S and that the experimentally obtained $E_{\rm act}$ corresponds to $d_c E_{\rm BL}$.

Based on this consideration, we study the Langevin dynamics of the magnetizations, i.e., we solve numerically the stochastic Landau-Lifshitz-Gilbert equation for the discretized model of the Hamiltonian, Eq. (2), including the perpendicular magnetization component n_z (see Appendix E). Figures 5(a), 5(c), and 5(e) show the snapshots of the in-plane magnetization configuration at each instant with color coding in the inset of Fig. 5(a). Figures 5(b), 5(d), and 5(f) show the corresponding $\varphi(\phi)$ (the same as shown in Fig. 1). These

figures show the time evolution of the helicity reversal via the creation of kink-antikink pairs and their successive pair annihilation. (see Movie S4). Figure 5(g) presents a schematic view of the kink-antikink (that is, a pair of BLs) formation across the potential barrier between the two stable states with different helicities, i.e., $\varphi = \pm\pi/2$.

IV. CONCLUSIONS

In conclusion, we have observed the thermal activation for skyrmion helicity reversals at temperatures above RT for bubbles with topological number -1 produced in a thin plate of a hexaferrite magnet. Systematic analyses of *in situ* LTEM movies demonstrate the decrease of kink energy and an increase of frequency for skyrmion helicity reversals with increasing temperature toward T_C. Both experimental results and simulations are in accord with each other to give the relatively small energy (e.g., $\sim$1 eV at $T = T_C - 15$ K) for the generation of the kink pair on the domain wall of the bubble. This work provides the basic information for controlling the topological magnetization texture.

ACKNOWLEDGMENTS

The authors thank M. Kawasaki and T. Arima for enlightening discussions. This work was supported in part by JSPS Grant-in-Aid for Scientific Research(S) Nos. 24224009, 15H03553, 15K05192, 24360036 and Nanotechnology Platform No. A-14-NM-0028 of the MEXT, Japan.

X.Z.Y. and K.S. contributed equally to this work.

APPENDIX A: TRANSPORT-OF-INTENSITY EQUATION

To determine the helicity of bubbles, we have obtained quantitative information on the in-plane magnetization. We have analyzed the defocused LTEM images by using a software package QPt (HREM Co.) [22], which is based on the transport-of-intensity equation (TIE),

$$\frac{2\pi}{\lambda}\frac{\partial I\,(xyz)}{\partial z} = \nabla_{xy}[I\,(xyz)\nabla_{xy}\varphi(xyz)], \qquad \text{(A1)}$$

and the Maxwell-Ampére equation,

$$\nabla_{xy}\varphi(xyz) = -\frac{e}{\hbar}(\boldsymbol{M}\times\boldsymbol{n})t. \qquad \text{(A2)}$$

Here, $I(xyz)$, $\phi(xyz)$, $\boldsymbol{M}$, t, and $\boldsymbol{n}$ represent the intensity, phase of the incident electron beam, the magnetization of the material, the sample thickness, and the unit vector perpendicular to the sample surface, respectively. The analysis of the gradient of electron beam intensity ($\frac{\partial I\,(xyz)}{\partial z}$) allows us to obtain the local magnetization textures of bubbles.

APPENDIX B: MAGNETIC PHASE DIAGRAM IN THE (001) BFSMO THIN PLATE

The TEM sample is subject to the normal magnetic field $B_z \approx \frac{B_0}{1+(z/a)^2}$ induced by gradual tuning of the magnetic-objective lens current of a microscope (FEI, TITAN Cubed). Here, B_0 is a field at the sample position of $z = 0$ and a is the focal length [21]. The parameters B_0 and a are determined by the objective lens current. The magnitude of the magnetic field at the sample position was measured in advance by a Hall probe as a function of the objective lens current.

First, the change of spontaneous magnetic structure with temperature is revealed as shown in Fig. 6(a), by the present LTEM observations as well as by the previous neutron studies [19]. The ferromagnetic transition occurs around 450 K and the uniaxial ferromagnetic structure turns into a conical structure with a modulation vector along the [001] axis at temperatures below 300 K.

Figures 6(b)–6(j) show the variations of magnetic configurations of the (001) thin plate with the bias fields applied perpendicularly to the plate plane. The LTEM images and TIE analyses indicate that the hexagonlike deformed bubbles with random helicity distribution form a triangular lattice at zero-bias field [Fig. 6(b)]. Such a bubble lattice changes to stripelike domains [Fig. 6(c)] with increasing bias field up to 40 mT. The formation of a triangular bubble lattice [Fig. 6(d)] appears again with further increasing bias field up to 110 mT, while the spacing between the bubbles becomes larger than that for the zero-bias-field situation. Interestingly, the bubble helicity reversals randomly occur when the bias field is reversed. The magnetic configurations change symmetrically in scanning the positive and negative bias fields, revealing the intrinsic nature of the zero-bias bubble lattice in the (001) BFSMO thin plate at RT.

APPENDIX C: PRINCIPAL COMPONENT ANALYSIS (PCA)

In order to extract quantitative information on bubble helicity dynamics, we apply principal component analysis (PCA) to the intensities of the bubbles in the LTEM movies by regarding each frame as a vector. Because bubble helicity reversal is supposed to be the largest contribution to the intensity change in the movies, the first principal eigenvectors are expected to correspond to the intensity distribution of a magnetic bubble and, hence, to be useful to evaluate magnetic helicity. The detailed procedures are as follows:

(1) We calculate intensity distribution averaged over all the frames at each temperature $I_{\rm avg}(\boldsymbol{r},T)(=\frac{1}{f_{\rm all}}\sum_f I(\boldsymbol{r},T,f))$, where I, $\boldsymbol{r}$, f, $f_{\rm all}(=201)$, and T are intensity, pixel position, frame number, total number of frames in a movie, and temperature, respectively.

(2) We allot a specific number n to each of the 66 bubbles shown in Fig. 3(a).

(3) For each n and T, we set a 71×71 pixel rectangular region of interest (ROI) so that it contains the intensity distribution $I\,(\boldsymbol{r},f,T,n)$ of the corresponding bubble and crop it as a movie.

(4) We transform each 71×71 pixel two-dimensional frame image in the cropped movies into a vector with 5041 elements, and apply PCA to all 201 vectors in each movie.

(5) For each n and T, we calculate a variance-covariance matrix whose (i,j) element is written as

$$M^{\rm cov}_{i,j}(T,n) = \frac{1}{f_{\rm all}}\sum_f [I(\boldsymbol{r}_i,T,n,f)I(\boldsymbol{r}_j,T,n,f)] - I_{\rm avg}(\boldsymbol{r}_i,T,n)I_{\rm avg}(\boldsymbol{r}_j,T,n), \qquad \text{(C1)}$$

where $I_{\rm avg}(\boldsymbol{r},T,n) = \frac{1}{f_{\rm all}}\sum_f I(\boldsymbol{r},T,n,f)$.

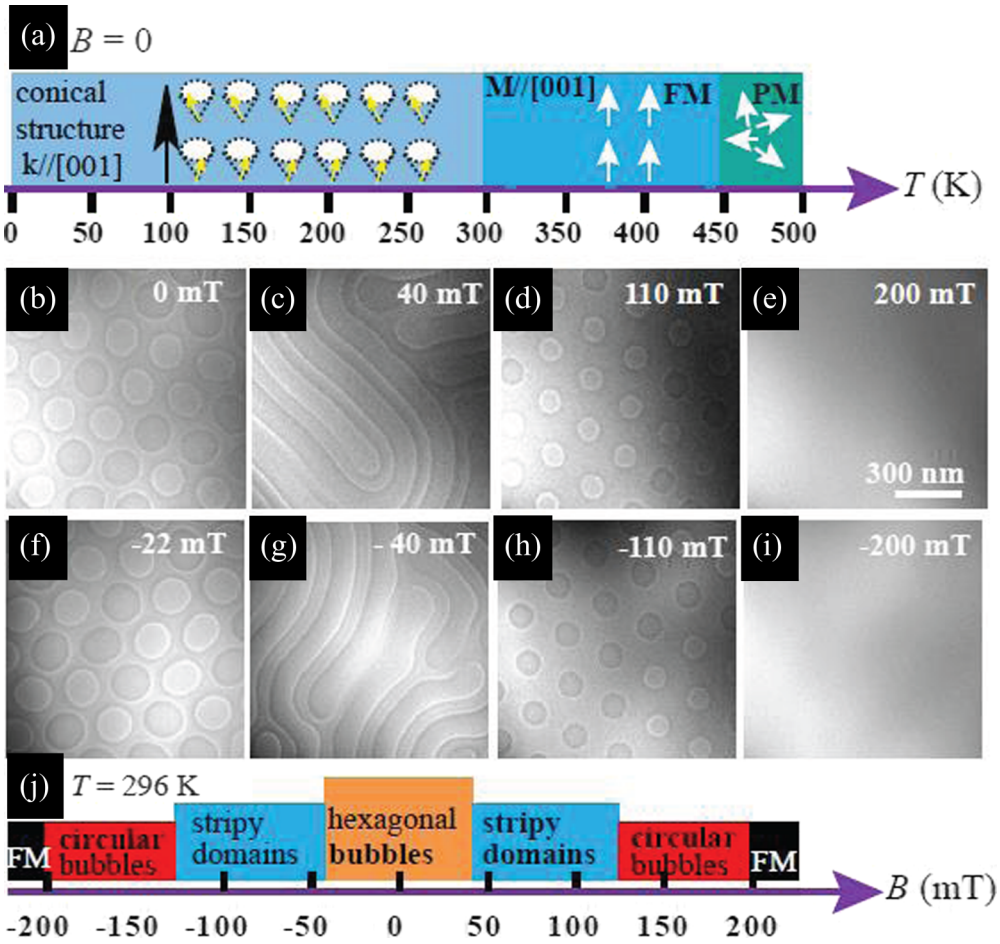

FIG. 6. Magnetic phase diagrams of $BaFe_{12-x-0.05}Sc_xMg_{0.05}O_{19}(x = 1.8)$. (a) Temperature dependence of magnetic structure in a (001) thin plate at $B = 0$. Short arrows, FM, and PM represent the magnetization direction, the ferromagnetic structure, and the paramagnetic structure, respectively. (b)-(i) Variations of magnetic domain structure with the bias fields which are applied normally to the (001) thin plate. (j) Changes of magnetic domain structure of the (001) thin plate at $T = 296$ K with bias fields.

(6) We calculate 5041 pairs of an eigenvalue $\lambda_k(T,n)$ and an eigenvector $E_k(\boldsymbol{r},T,n)$ for each $M_{i,j}^{\mathrm{cov}}(T,n)$, where k is the index of the eigenvalue and the eigenvector. Since the eigenvalue of the covariance matrix corresponds to the relative contribution to deviation, the eigenvector $E_0(\boldsymbol{r},T,n)$ with the largest eigenvalue $\lambda_0(T,n)$ is the first principal component for the intensity deviation in the movies. In this analysis, $E_0(\boldsymbol{r},T,n)$ should correspond to the intensity distribution of a bubble since bubble helicity reversal is supposed to be the largest contribution to the intensity change.

(7) We transform $E_0(\boldsymbol{r},T,n)$ into a 71×71 pixel image by the inverse process in step (4) and check if the images present intensity distributions of a bubble or not. Typical transformed images are shown in Figs. 3(b) and 3(d). We neglect any eigenvector which does not present an intensity distribution of a bubble.

(8) For $E_0(\boldsymbol{r},T,n)$, which presents the intensity distribution of a bubble, we retake its sign so that its transformed image presents the intensity distribution of a bubble with + helicity.

(9) For each n, T, and f, we obtain a score $l(f,T,n)$ along the first principal axis by calculating the inner product between the first principal eigenvector $E_0(\boldsymbol{r},T,n)$ and the intensity difference from the average $I_{\mathrm{avg}}(\boldsymbol{r},T,n)$ as

$$l(f,T,n) = \sum_{i=1}^{5041}[E_0(\boldsymbol{r}_i,T,n) \times \{I(\boldsymbol{r}_i,T,n,f) - I_{\mathrm{avg}}(\boldsymbol{r}_i,T,n)\}]. \quad \text{(C2)}$$

(10) The obtained score $l(f,T,n)$ corresponds to the deviation due to the helicity reversal; however, $l(f,T,n) = 0$ does not correspond to the middle between the + and − configurations. Since $I_{\mathrm{avg}}(\boldsymbol{r},T,n)$ does not generally correspond to the middle value due to asymmetric dwell time for the + and − configurations, the sign of $l(f,T,n)$ does not always conform to the sign of the frame-averaged helicity. Thus, we correct the center of helicity deviation of $l(f,T,n)$, assuming symmetric deviation for the both helicities. We obtain the center-corrected score h as $h(f,T,n) \equiv l(f,T,n) - l_0(T,n) = 0$. Here, $l_0(T,n) \equiv \frac{\max\{l(f,T,n)|f\} - \min\{l(f,T,n)|f\}}{2}$ is the middle value of the $l(f,T,n)$ between the maximum and minimum of $l(f,T,n)$ in the 201 frames.

(11) We plot the score $h(f,T,n)$ from 700 to −700 in the blue-white-red gradation as shown in Fig. 3(e).

(12) The principal eigenvectors without the intensity distribution corresponding to a bubble are neglected in step (6) above due to the following reasons: (A) The time of helicity reversal τ_c is comparable or shorter than the exposure time for each frame in LTEM movie. These cases should weaken the averaged intensity of both the + bubble and − bubble to be comparable to the noise level. (B) The drifting motion or deformation of the target bubble occurs for the duration of the movie. (C) No intensity change owing to helicity reversal in the movie duration.

In cases (A) and (B) above, since no information on helicity reversal can be obtained, we plot them in gray in Fig. 3(e) to indicate undeterminable helicity. Meanwhile, in case (C), we plot the corresponding helicity, which is identified by the intensity distribution in the LTEM movie.

APPENDIX D: MONTE CARLO CALCULATIONS

To discuss the activation energy $E_{\rm act}$ for the helicity reversal of the bubbles, we estimate quantitatively the helicity-reversal time $\tau(T)$ by analyzing LTEM movies. Based on the Arrhenius law $\tau(T) \propto \exp\{\frac{E_{\rm act}(T)}{k_B T}\}$, we can estimate $E_{\rm act}$, which is proportional to the square of the effective magnetic moment (m) and should decrease with increasing temperature. The detailed procedures are as follows:

(1) We focus on a typical bubble (No. 3) and plot the averaged intensity of the inner ring as a function of time (frame) [shown in Fig. 4(a)].

(2) We obtain the histograms of the averaged intensity of the bubble for all frames in the LTEM movie at various temperatures [shown in Fig. 4(b)].

(3) Assuming that the helicity reversal occurs in a Poisson random process with parameter τ_c, we carry out Monte Carlo calculations to obtain the histogram of the frame-averaged intensity for various ratios between τ_c and exposure time $\tau_{\rm exp}$ [shown in Fig. 4(c)].

(4) We estimate the temperature dependence of the helicity-reversal time $\tau(T)$ as shown in Fig. 4(d) by comparison with the results of Monte Carlo calculations [shown in Fig. 4(c)] and the histograms of averaged intensities [shown in Fig. 4(b)].

(5) From the slopes of $\tau(T)$ shown as the dashed lines in Fig. 4(d), we estimate the range of $E_{\rm act}$ based on the Arrhenius law $\tau(T) \propto \exp\{\frac{E_{\rm act}(T)}{k_B T}\}$ as

$$430 k_B |T_C - T| < E_{\rm act}(T) < 1300 k_B |T_C - T|. \quad \text{(D1)}$$

APPENDIX E: MODELING AND SIMULATIONS

We examine the helicity reversal of a magnetic bubble using a simplified model appropriate for the high-Q limit, where $Q = K/(2\pi M^2)$ with dipolar coupling $2\pi M^2$, and anisotropy energy K [12]. The magnetic bubble is supposed to be a circular, cylindrical magnetic domain structure where the two ferromagnetic regions, i.e., inside and outside of the cylinder, are divided by a magnetic domain wall (DW). The width of the DW is characterized by $\xi = \sqrt{A/K}$, where A is the ferromagnetic exchange energy. The magnetic moments $\boldsymbol{n}$ are uniform through the z direction and can be written as

$$\begin{aligned}\boldsymbol{n}(\boldsymbol{r}) &= \cos\varphi(\phi)\sin\theta_r \boldsymbol{e}_r + \sin\varphi(\phi)\sin\theta_r \boldsymbol{e}_\phi + \cos\theta_r \boldsymbol{e}_z \\ &= n_r(\boldsymbol{r})\boldsymbol{e}_r + n_\phi(\boldsymbol{r})\boldsymbol{e}_\phi + n_z(\boldsymbol{r})\boldsymbol{e}_z, \end{aligned} \quad \text{(E1)}$$

where $\boldsymbol{n}(\boldsymbol{r})$ is the direction of the magnetic moment, the angle $\varphi(\phi)$ represents the in-plane magnetic texture and is measured from the radius direction, and $\{\boldsymbol{e}_r, \boldsymbol{e}_\phi, \boldsymbol{e}_z\}$ is the basis set for $\boldsymbol{n}(\boldsymbol{r})$ in the $r\phi z$-coordinate system, i.e., $n_r(\boldsymbol{r})[n_\phi(\boldsymbol{r})]$ is the in-plane component of $\boldsymbol{n}(\boldsymbol{r})$ along (perpendicular to) the radius direction and $n_z(\boldsymbol{r})$ denotes the out-of-plane component of $\boldsymbol{n}(\boldsymbol{r})$. The anisotropy energy is defined as $-K(n_z)^2$, and results in the DW solution θ_r,

$$\theta_r = \pm 2 \arctan \exp\left(\frac{r - R}{\xi}\right), \quad \text{(E2)}$$

with the bubble radius R ($\gg \xi$).

The model Hamiltonian considered here is given by

$$H = d_c \int d^2 r [A(\nabla \boldsymbol{n})^2 - 2\pi M^2 (n_\phi)^2], \quad \text{(E3)}$$

where d_c is the number of layers perpendicular to the sample. The $A > 0$ favors the ferromagnetic configurations and the second term represents the stability of the Bloch wall structure, $\varphi(\phi) = \pm\pi/2$. With these assumptions, we find the effective Hamiltonian for the in-plane magnetic moments in the DW,

$$H = 2\xi d_c \oint d\phi \left\{ \frac{1}{R} A[\partial_\phi \varphi(\phi)]^2 - 2\pi M^2 R \sin^2 \varphi(\phi) \right\}, \quad \text{(E4)}$$

and here we use $\int dr \sin^2\theta_r = 2\xi$.

The Hamiltonian, Eq. (E4), is reduced into the model on a one-dimensional chain of the normalized magnetic moments $\boldsymbol{n}_i$ as shown in Fig. 5(a) for $\phi = 2\pi i/N (i = 0 \sim N-1)$,

$$H = -J \sum_{i=0}^{N-1} (n_{x,i} n_{x,i+1} + n_{y,i} n_{y,i+1}) - C \sum_{i=0}^{N-1} (n_{\phi,i})^2, \quad \text{(E5)}$$

with $n_{x,i} = \boldsymbol{n}_i \cdot \boldsymbol{e}_x$, $n_{y,i} = \boldsymbol{n}_i \cdot \boldsymbol{e}_y$, and $n_{\phi,i} = \boldsymbol{n}_i \cdot \boldsymbol{e}_\phi$, ferromagnetic interaction J, and uniaxial anisotropy C along $\boldsymbol{e}_\phi$. Using this Hamiltonian, Eq. (E5), we numerically study the helicity-reversal problem by the stochastic Landau-Lifshitz-Gilbert equation,

$$(dn_r)/dt = \gamma[-\partial H/(\partial n_r) + h_{(T,r)}(t)] \times n_r + \alpha n_r \times (dn_r)/dt, \quad \text{(E6)}$$

where $\boldsymbol{h}_{T,\boldsymbol{r}}(t) = [h_{T,\boldsymbol{r},x}(t), h_{T,\boldsymbol{r},y}(t), h_{T,\boldsymbol{r},z}(t)]$ is the Gaussian noise field, with the statistical properties $\langle \boldsymbol{h}_{T,\boldsymbol{r}}(t) \rangle = \boldsymbol{0}$ and $\langle h_{T,\boldsymbol{r},\mu}(t) h_{T,\boldsymbol{r}',\nu}(t) \rangle = 2k_B T \alpha \delta_{\mu\nu} \delta(\boldsymbol{r} - \boldsymbol{r}) \delta(t - t')$, for the finite temperature effect. The gyromagnetic ratio and the Gilbert damping constant are denoted by γ and α, respectively. This model has twofold degenerate ground states corresponding to the Bloch wall states with a helicity degree of freedom, and the states are represented by $\varphi(\phi) = \pm\pi/2$ (see Fig. 5).

Figure 5 shows an example of the numerical result with a parameter set $\{N = 200, C/J = 0.01, \alpha = 0.01, k_B T/J = 0.06\}$. Hereafter, the unit of time t is typically ∼0.7 ps for $J = 1$ meV. For the Langevin dynamics, we set a sufficiently long thermalization period, e.g., 20 000, using the initial state $\varphi(\phi) = +\pi/2$, and after the thermalization period, we examine the real-time dynamics of the helicity reversal. Along

the time evolution, the dynamics shows the relatively long stay (the duration is 3000 or more) at the state $\varphi(\phi) \approx +\pi/2$ or $-\pi/2$ and the rapid transition between them by the fluctuation due to the random torque $\boldsymbol{h}_{T,\boldsymbol{r}}(t)$. Figure 5(a) shows a snapshot at a time where the stay at $\varphi(\phi) \approx +\pi/2$ is almost ended and a transition to the state $\varphi(\phi) \approx -\pi/2$ begins. We measure the time t from this point. In the figure, 20 magnetic moments out of $N = 200$ are presented by the arrows, and the color specifies the angle $\varphi(\phi)$. Figures 5(c) and 5(e) and 5(d) and 5(f) represent the magnetic structures [profiles of the angle $\varphi(\phi)$] at $t = 320$ and 600, respectively. In this numerical result, the change in magnetic texture occurs at a local region at around $\phi \sim -\pi/3$ in the beginning [see the snapshot at $t = 320$ and the corresponding angle $\varphi(\phi)$ shown in Figs. 5(c) and 5(d)]. The *deflection* region becomes wider and wider, and eventually the transition to the state $\varphi(\phi) \approx -\pi/2$ is achieved. The transition from Fig. 5 (a) [Fig. 5(b)] to Fig. 5(e) [Fig. 5(f)] occurs within a time period of ∼600.

The numerical results shown in Fig. 5 indicate that the helicity reversal occurs through the pair creation and annihilation of the BLs. This is described by the kink-antikink pair creation and annihilation in the profile of the angle $\varphi(\phi)$.

We evaluate the creation energy of the BLs using the Hamiltonian, Eq. (E4). The kink solution in the angle $\varphi(\phi)$ corresponds to the BL with a width $\lambda = \sqrt{A/(2\pi M^2)}$ and it costs an energy $E_{\rm BL} = 8 d_c A Q^{-1/2}$. The ferromagnetic exchange energy A is defined for the normalized magnetic moments and, hence, at around critical temperature $T \sim T_C$, it is substituted as

$$A \Rightarrow A_0 \left(1 - \frac{T}{T_C}\right), \tag{E7}$$

where A_0 is the low-temperature ferromagnetic exchange energy. A mean field approximation gives $A_0 = k_B T_C$, so that

$$E_{\rm BL} = 8 d_c (k_B T_C) \left(1 - \frac{T}{T_C}\right) \frac{1}{\sqrt{Q}}. \tag{E8}$$

For $T_C = 450\,\mathrm{K}$, Eq. (E8) results in

$$E_{\rm BL} = (0.3\ \mathrm{eV}) d_c \frac{1}{\sqrt{Q}} \left(1 - \frac{T}{T_C}\right), \tag{E9}$$

which leads to the estimation of $d_c E_{\rm BL} \approx 1.8\,\mathrm{eV}$ in the text.

[1] M. Yamanouchi, D. Chiba, F. Matsukura, and H. Ohno, Nature (London) **428**, 539 (2004).

[2] S. S. P. Parkin, M. Hayashi, and L. Thomas, Science **320**, 190 (2008).

[3] A. H. Bobeck and H. E. D. Scovil, Sci. Am. **78**, 224 (1971).

[4] A. H. Eschenfelder, *Magnetic Bubble Technology*, Springer Series in Solid-State Sciences Vol. 14 (Springer, Berlin, 1980).

[5] N. Nagaosa and Y. Tokura, Nat. Nanotechnol. **8**, 899 (2013).

[6] S. Mühlbauer, B. Binz, F. Jonietz, C. Pfleiderer, A. Rosch, A. Neubauer, R. Georgii, and P. Böni, Science **323**, 915 (2009).

[7] X. Z. Yu, Y. Onose, N. Kanazawa, J. H. Park, J. H. Han, Y. Matsui, N. Nagaosa, and Y. Tokura, Nature (London) **465**, 901 (2010).

[8] Y. Tokunaga, X. Z. Yu, J. S. White, H. M. Rønnow, D. Morikawa, Y. Taguchi, and Y. Tokura, Nat. Commun. **6**, 7638 (2015).

[9] A. Fert, V. Cros, and J. Sampaio, Nat. Nanotechnol. **8**, 152 (2013).

[10] W. Jiang, P. Upadhyaya, W. Zhang, G. Yu, M. B. Jungfleisch, F. Y. Fradin, J. E. Pearson, Y. Tserkovnyak, K. L. Wang, O. Heinonen, S. G. te Velthuis, and A. Hoffmann, Science **349**, 283 (2015).

[11] X. Yu, M. Mostovoy, Y. Tokunaga, W. Zhang, K. Kimoto, Y. Matsui, Y. Kaneko, N. Nagaosa, and Y. Tokura, Proc. Natl. Acad. Sci. USA **109**, 8856 (2012).

[12] A. P. Malozemoff and J. C. Slonczewski, *Magnetic Domain Walls in Bubble Materials* (Academic, New York, 1979).

[13] A. Hubert and R. Schäfer, *Magnetic Domains* (Springer, Berlin, 1998).

[14] A. Rosch, Proc. Natl. Acad. Sci. USA **109**, 8793 (2012).

[15] S. R. Logan, J. Chem. Educ. **59**, 279 (1982).

[16] H. B. Braun, Adv. Phys. **61**, 1 (2012).

[17] H. B. Braun, Phys. Rev. Lett. **71**, 3557 (1993).

[18] M. Nagao, Y.-G. So, H. Yoshida, M. Isobe, T. Hara, K. Ishizuka, and K. Kimoto, Nat. Nanotechnol. **8**, 325 (2013).

[19] Y. Tokunaga, Y. Kaneko, D. Okuyama, S. Ishiwata, T. Arima, S. Wakimoto, K. Kakurai, Y. Taguchi, and Y. Tokura, Phys. Rev. Lett. **105**, 257201 (2010).

[20] L. Reimer and H. Kohl, *Transmission Electron Microscopy* (Springer, New York, 2007).

[21] X. Yu, A. Kikkawa, D. Morikawa, K. Shibata, Y. Tokunaga, Y. Taguchi, and Y. Tokura, Phys. Rev. B **91**, 054411 (2015).

[22] K. Ishizuka and B. Allman, J. Electron Microsc. **54**, 191 (2005).

[23] See Supplemental Material at http://link.aps.org/supplemental/10.1103/PhysRevB.93.134417 for *in-situ* LTEM movies.

[24] K. Pearson, Philos. Mag. **2**, 559 (1901).